Fast scanning probe for the NSTX spherical tokamak

J. A. Boedo,[1] N. Crocker,[1] L. Chousal,[1] R. Hernandez,[1] J. Chalfant,[1] H. Kugel,[2] P. Roney,[2] J. Wertenbaker,[2] and NSTX Team[a)]
[1]*Department of Mechanical and Aerospace Engineering, Energy Research Center, University of California, San Diego, La Jolla, California 92093-0417, USA*
[2]*Princeton Plasma Physics Laboratory, Princeton, New Jersey 08543, USA*

(Received 4 November 2008; accepted 26 October 2009; published online 31 December 2009)

We describe a fast reciprocating Langmuir probe and drive system, which has four main new features: (1) use of high-temperature, vacuum, circuit boards instead of cables to reduce weight and increase to 21 the number of possible connections, (2) rotatable and removable shaft, (3) 10 tip construction with designed hardware bandwidth up to 10 MHz, and (4) a detachable and modular tip assembly for easy maintenance. The probe is mounted in a fast pneumatic drive capable of speeds ~ 7 m/s and $\sim 20g$'s acceleration in order to reach the scrape-off layer (SOL) and pedestal regions and remain inserted long enough to obtain good statistics while minimizing the heat deposition to the tips and head in a power density environment of 1–10 MW/m^2. The National Spherical Torus Experiment SOL features electron temperature, $T_e \sim 10-30$ eV, and electron density, $n_e \sim 0.1-5 \times 10^{12}$ cm^{-3} while the pedestal features $n_e \sim 0.5-1.5 \times 10^{13}$ cm^{-3} and $T_e \sim 30-150$ eV. The probe described here has ten tips which obtain a wide spectrum of plasma parameters: electron temperature profile $T_e(r)$, electron density profile $n_e(r)$ and Mach number profile $M(r)$, floating potential $V_f(r)$, poloidal and radial electric field profiles $E_\theta(r)$ and $E_\rho(r)$, saturation current profile $I_{sat}(r)$, and their fluctuations up to 3 MHz. We describe the probe and show representative radial profiles of various parameters. © *2009 American Institute of Physics.* [doi:10.1063/1.3266065]

I. INTRODUCTION

Probes have been utilized very successfully for long to diagnose plasmas, ranging from small experiments to large fusion devices. The tokamak is a magnetic confinement device and a leading candidate for developing an energy source based on magnetic fusion. Spherical tokamaks[1] are a relatively new class of devices exploring an operating space that could have advantages for future reactors.[2]

In a tokamak, the plasma core, where the fusion reactions occur, eventually establishes contact with the walls of the containment device via a region called the scrape-off layer (SOL). Understanding of the SOL has profound implications for future fusion devices since their performance is limited by the heat and particle loads on the plasma-facing wall,[3] and because the tokamak plasma edge is key to core performance.[4–9]

The need for predictive capability is driving an effort in plasma modeling[10–14] which requires a database of high spatial resolution edge/SOL data for validation and scaling purposes and to develop understanding of how energy and particles are transported.[15]

Probes have been extensively used in magnetic confinement devices[16–19,9,20–31] in the past 50 years; the original designs were stationary,[9] but as the performance of the devices increased, fast probe systems (5 m/s) on reciprocating drives[19] in the 1980s were developed to cope with the rapidly increasing heat and particle loads and most probe systems built since have followed that concept with some variations. Original fast scanning probe designs were all metal construction[19,9,20] (steel or tungsten) with 2–4 tungsten tips. The metal would erode (by chemical or physical sputtering) resulting in the release of high Z materials into the plasma core and reducing performance, therefore graphite and ceramic designs were developed.

The complexity of the plasma phenomena and versatility of probes led to a demand for more sensors with higher bandwidth in the probe heads and for a need to probe deeper (2–5 cm) inside the plasma. Consequently, modern designs address additional constrains imposed on probe systems include minimization of plasma contamination, the presence of large electric fields while reducing the probe perturbation (i.e., size). Designs for DIII-D,[18,21] PBX-M,[9] TEXTOR,[22] ASDEX,[29,30] TCV,[26] JET,[27,28] TFTR,[31,12,33] and MAST (Ref. 25) are mostly graphite and boron nitride (BN) construction. Some of the designs (DIII-D, JET, TFTR, etc.) include a detachable head for ease of repair and versatility and to optimize the use of the limited number of conductors available due to space constrains, which vary widely[25] although a common number is five.[18,26] Spherical tokamaks in general, and National Spherical Tokamak Experiment (NSTX) in particular, are a new class of devices, and there is a dire need to characterize the edge/SOL region.

Plasma parameters in tokamaks vary greatly across the edge,[12] from core values ($T_e \sim 1-10$ keV and $n_e \sim 1-5 \times 10^{19}$ m^{-3}) to edge/SOL values ($T_e \sim 10$ eV and $n_e \sim 5 \times 10^{17}$ m^{-3}) in 15–20 mm across the last closed magnetic surface (or separatrix), thus measurements require high spa-

[a)]For a full listing of names and affiliations of the NSTX Team, see Addendum, Rev. Sci. Instrum. 80, 129901 (2009).

tial resolution (1–2 mm) and diagnostic density (T_e, n_e, E_r, E_θ, etc.) that can be provided almost exclusively by probes. The main criteria for the probe design are given by plasma conditions and access constraints. The design requirements can be summarized as:

(1) ability to obtain the needed measurements,
(2) increase the number of sensors/measurements at the probe head to provide measurements of $T_e(r)$, $n_e(r)$, poloidal electric field $E_\theta(r)$, radial electric field $E_r(r)$, plasma Mach number $M(r)$, and flow $V_\parallel(r)$, profiles with 1–2 mm spatial resolution,
(3) cover the needed dynamic range ($T_e \sim 10-100$ eV, $n_e \sim 0.2-5\times10^{19}$ m^{-3}, $E_\theta \sim 0-80$ V/m, $E_r(r)$ 0–10 kV/m,
(4) profiles of fluctuation levels in n_e, $E_\theta(r)$, and $E_r(r)$, that have a bandwidth of $\sim$100–250 kHz, requiring sampling at $\sim$1 MS/s,
(5) survive the plasma conditions,
(6) head and tips should withstand a heat flux of $\sim 1-10$ MW/m^2 for up to $\sim$80 ms while keeping the graphite head and tips temperature below 1600 °C,
(7) be compatible with a base pressure of 1×10^{-8} Torr and bakeable to 150 °C,
(8) hold a potential of 3 kV to ground,
(9) be made of low Z materials so as not to contaminate the plasma due to ablation of the probe materials upon plasma exposure,
(10) withstand accelerations of up to $\sim 20g$. This is required to move the probe up to $\sim$3 m/s and keep the in-plasma exposure time under $\sim$40 ms, and
(11) access and ease of maintenance.

Access to diagnostics in tokamaks is difficult during operations due to the presence of radiation, rf, high voltage, and time constraints; therefore, the probe should be remotely operated and incorporate a design that is as reliable and simple as possible and geared to ease tips and head replacement.

We will devote this paper to the description of a probe system for NSTX (Ref. 32) that meets the requirements described and features:

(1) novel use of internal vacuum circuit boards to: (a) increase the number of internal connections to 21 and accommodate many sensors, (b) replace bulky coaxial cables, (c) simplify front and back feedthrough design, (d) assuring high signal bandwidth, and (e) reducing weight, volume, and vacuum pumping time,
(2) modular shaft which is easy to replace and rotate to match changes in the magnetic configuration,
(3) modular head and tip design, also using circuit boards, that allows more sensors and fast maintenance of the presently used 10 tips,
(4) industry standard modular control system based on programmable logic controller (PLC) controls and RS-232 terminals, and
(5) high-speed reciprocation (up to 3 m/s) and high heat flux capability (up to 10 MW/m^2).

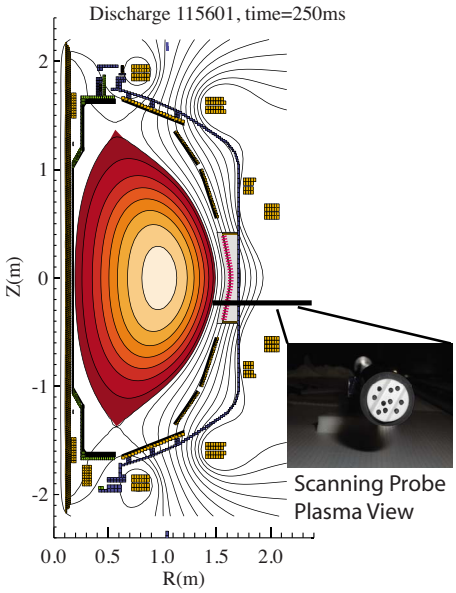

FIG. 1. (Color online) Poloidal cross section of the NSTX device showing the magnetic configuration. A horizontal line indicates the trajectory of the probe, slightly below the midplane, and an inset shows the probe head as seen from the plasma side.

II. SYSTEM DESCRIPTION

The system is located $\sim$0.19 m below the midplane in the low field side of the NSTX spherical tokamak, as seen in Fig. 1, and the probe features a total of 10 tips, as shown in the inset.

The general operating philosophy is that a probe shaft, containing the sensors, is quickly plunged into the plasma by a fast acting pneumatic reciprocating mechanism mounted on a carriage that is moved toward the plasma to a standby position by a slow mechanism. Therefore, the instrument assembly consists of two main parts: the drive mechanism (fast and slow) and the probe itself, all mounted on an aluminum backbone resting on an aluminum support, as shown in Fig. 2. The instrument interfaces to NSTX thru a 6 in. (15.2 cm) Conflat flange with a 3.8 in. (9.7 cm) bore internal diameter. A bellows is placed between the probe and a gate valve in order to absorb machine expansion and vibration. The system is differentially pumped before opening it to the machine, which assumes the pumping during operations. The local pressure is monitored with an ion gauge.

III. PROBE

The probe itself is composed of the head, shaft, and rear feedthrough, as shown in Fig. 3, and should be lightweight in order to maximize acceleration and decrease the forces generated during operation. The probe head and tips [Fig. 3(a)] are exposed to the plasma particle and heat flux repeatedly for $\sim$40–80 ms, resulting in erosion, thermal stress, and arcing damage and therefore the general design philosophy is to make them replaceable. The head holds the tips, which are exposed to the plasma, and bolts into the shaft as shown in Figs. 2(a) and 2(b). The signals are then transmitted inside the shaft (traditionally using coaxial cables) and come to air via the rear feedthrough as seen in Fig. 2(c).

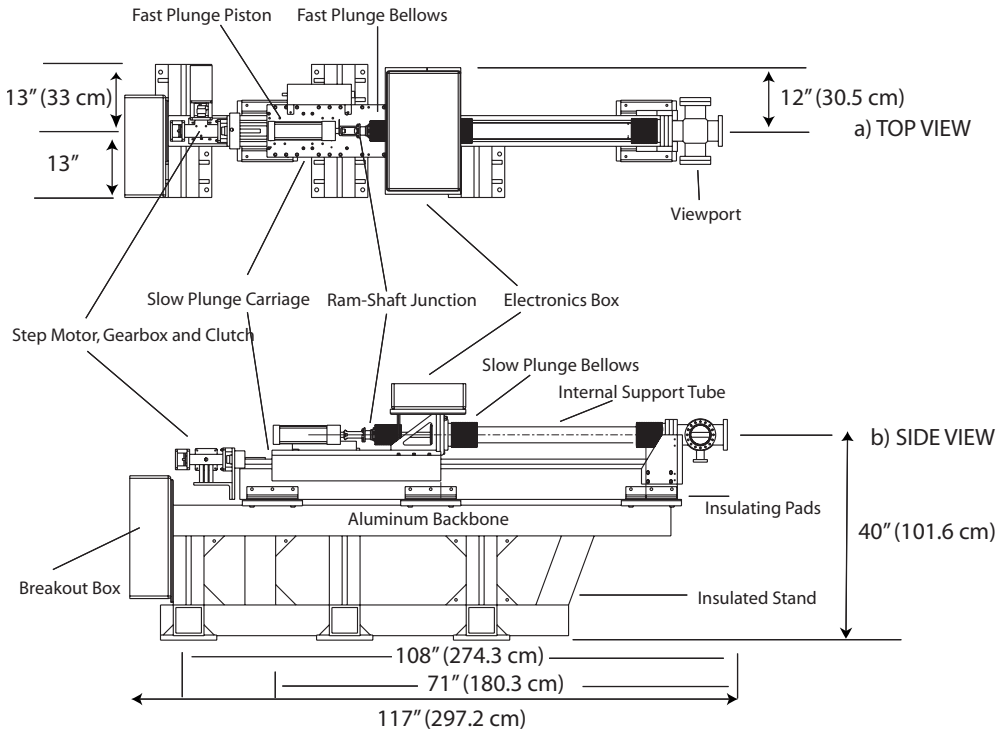

FIG. 2. CAD drawing indicating the main probe system components. The shaft and propelling piston move on top of a carriage that rides on parallel rails moved by a step motor. The probe system is supported by an aluminum backbone and is electrically insulated in two stages to prevent possible arcing. A breakout box provides easy access to all the cables and control system interface.

A. Probe head

The purpose of the head is to hold and shield ten tips made out of Thermalgraph carbon fiber composite (CFC) (with parallel thermal conductivity of 900 W/mK, twice as much as copper) mounted on a BN matrix for electrical insulation, as shown in Figs. 4(a) and 4(b). The whole structure is protected against high heat fluxes by a graphite shroud [Figs. 3(a) and 4(a)], except a small BN section [Fig. 3(a)] to prevent the graphite shroud (a conductor) from short circuiting the plasma. The exposed dimensions of the tips, which are filed to a tolerance of 0.1 mm in length by using a filing jig, are 1.6 mm length l and 1.5 mm diameter d. The approach taken in our head design is shown on Figs. 4–6 and it consists of four removable BN sections providing electrical insulation, thermal conduction, and mechanical strength in addition to two Vespel pieces to integrate the circuit board connections. The design[22] is mostly driven by the need to account for constant wear on the head and tips, which make it mandatory to periodically replace the tips and occasionally, the front BN insulator and graphite shield.

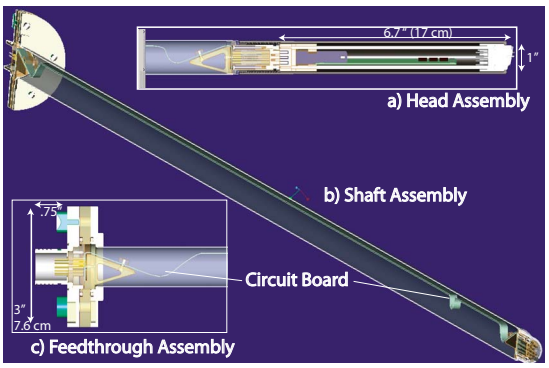

FIG. 3. (Color online) Entire shaft and head assembly overview. The CAD drawings show: (a) head and tip assembly and connector to the shaft, (b) shaft assembly showing the connector, shaft circuit board, and rear feedthrough assembly, and (c) detail of the rear flange, feedthrough, and connector assembly, highlighting the circuit board assembly; notice the simplicity of the connector achieved by the use of circuit boards.

The front BN piece [seen in Figs. 5 and 6(a)] is often heavily damaged/coated by the plasma, so it was designed to be easily extracted by merely *removing the graphite shield that holds it in place* [Fig. 3(a)] by unscrewing it from the shaft. The carbon composite tips can be replaced without a full head disassembly since they are held in place by M1 screws [Figs. 5 and 6(b)] on the back and further secured by steps in the front BN piece. Tip replacement is achieved by removing the front BN piece and unscrewing the tips from the rods.

A second BN piece encases the tip/board interface, partially made of Vespel, and the last two BN pieces form a clamshell that encases the circuit board itself as shown in Figs. 5 and 6(b). All the BN pieces are keyed to prevent rotation during assembly and operation. The head assembly is held in place by two long screws (Figs. 5 and 6) and also by the graphite shield, which is screwed onto the Inconel shaft at $M22\times1.5$. The electrical connections are made via pin-socket pairs held in the front and back Vespel matrix (Figs. 5 and 6) forming back and front connectors. Polyimide (Vespel trademark by Dupont) is an easy-to-machine material, lightweight, and strong (85–95 Rockwell H), resists high temperatures (300 °C) and has a very low outgassing rate[33] (4×10^{-10} Torr-l/s cm^2 at room temperature and 3×10^{-6} at

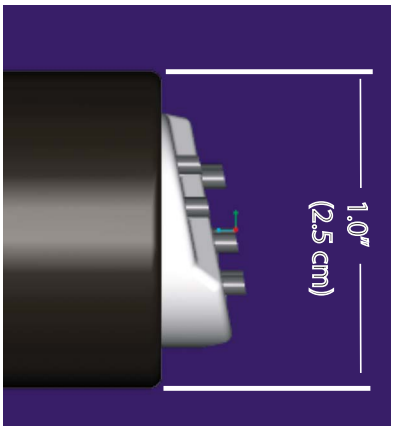

a) Side View

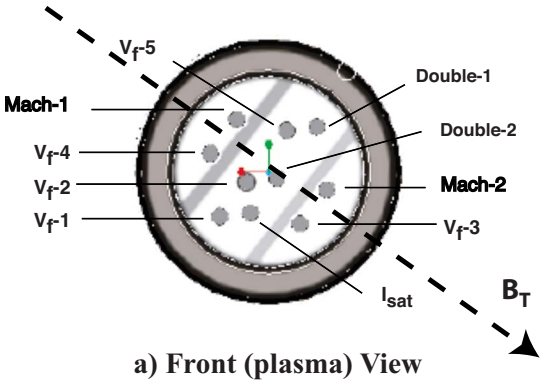

a) Front (plasma) View

FIG. 4. (Color online) Probe tip geometry. Side view (a) showing the proud tip and recessed-tip geometry and the face cut following the flux surface geometry. (b) Front head view with tips labeled according to their function. Tips V_{f1} to V_{f5} are at floating potential, two tips labeled Double1 and 2 are in a double probe configuration, two more tips measure the Mach number of the plasma flow and a last tip measures I_{sat}. The toroidal magnetic field B_T is sloping at ~35° as seen from the inside of the vessel.

300 °C). Vespel is slightly hygroscopic and absorbs water upon air exposure, which is then released during bakeout; therefore Vespel is used within a highly vented probe shaft to allow pumping.

The probe tips are aligned with the magnetic field as seen in Fig. 4(b), in such a manner that magnetic field angle can vary ±7° from nominal without mutual tip shadowing

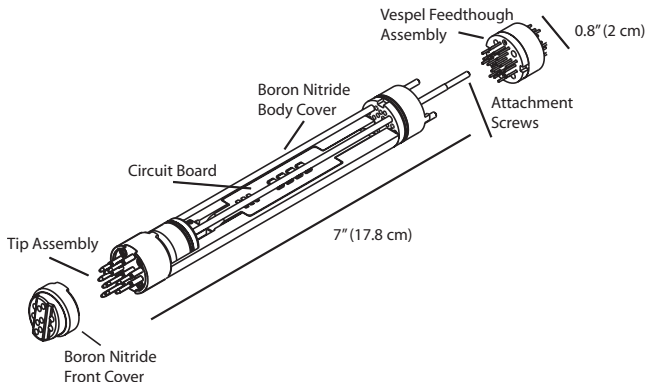

FIG. 5. CAD drawing showing a head overview with the main components (BN shells, Vespel connectors, circuit board, and tip assembly), and the attachment screws holding it together. Notice the screw-in tip assembly and easily removable BN tip cover.

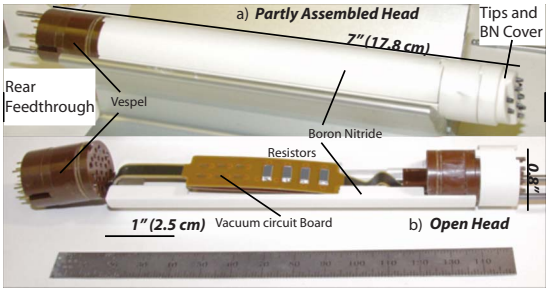

FIG. 6. (Color online) Probe head assembly: (a) the whole head assembled with the front BN and tip section, and (b) open, without the tips or front BN assembly, showing the connector assembly, the circuit board and the clam-shell BN design. Note the flexible board that facilitates assembly.

yet allowing them to sample approximately the same plasma. The usual NSTX magnetic field pitch angle is ~38° at the edge but the shaft is rotatable to accommodate I_p and B_t changes Since the probe is located 20.3 cm below the NSTX midplane the flux surfaces move away in the poloidal direction (Fig. 1), and, therefore, the probe face and tips need to follow that contour, which is ~11° from the vertical on the average, as shown in Fig. 4(a). Two tips [Double-1 and Double-2 in Fig. 4(b)] are used as a double probe pair, one tip is at ion saturation (I_{sat}), three proud, poloidally separated tips (V_{f1}, V_{f2}, and V_{f5}) are floating to measure the floating potential (and, by subtraction, the poloidal electric field), tips V_{f3} and V_{f4} are also floating and displaced 1.6 mm radially from V_{f2} to measure the radial electric field and tips Mach-1 and Mach-2 are at saturation current to measure parallel plasma flow. The floating tips have a 100 kΩ resistor (much higher than the plasma sheath impedance) in series to ground that are located in the head circuit board [Figs. 5 and 6(b)].

B. Head and shaft circuit boards

An innovative element of this probe design is the use of high vacuum, high temperature printed circuit boards that offer a threefold advantage:

(1) reduces the complexity in design and assembly by eliminating crimping, fastening, and cutting to size of cables,
(2) provides a compact platform to install sensors and other components such as resistors, and
(3) reduces the weight of the probe shaft and head.

The circuit boards used in both the probe and shaft are made of Pyralux FR-9120, a Polyimide-based material that is vacuum compatible, can be baked to ~200 C, encasing multiple layers of oxygen-free copper traces. The boards are designed to keep ~50 Ω impedance and consist of alternate signal, dielectric, and ground layers to keep cross talk low and reduce noise levels. A typical board layering contains: 1 mil Polyimide cover film layer, Cu ground plane, 7 mils Polyimide dielectric layer, 7.5 mil Cu signal traces layer, 4 mils Polyimide dielectric layer, 7.5 mils Cu signal layer, 7 mils Polyimide dielectric layer, Cu ground plane, and 1 mil Polyimide cover film. The signal trace layer has alternate ground traces to construct the equivalent of a coaxial cable and have been tested to 3 kV voltage standoff. The signal traces are designed to withstand repeated current pulses of 4

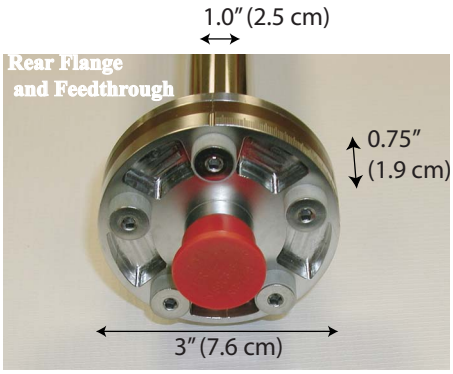

FIG. 7. (Color online) Rear shaft, showing the compact (0.75 in.=2.5 cm thick) assembly containing the feedthrough and flanges with the Vespel seal between them.

A for 50 ms at 1 min duty cycle (more stringent than the 10 min NSTX pulse cycle) and to operate at a continuous 100 °C without long-term degradation.

Both the head and shaft boards and the connectors are designed to carry 21 signals although in the middle of the head the connections go down to 10, the number of pins commissioned so far and the rest of the connections end in contact pads, seen in Fig. 6(b) next to the resistors, that can be used for any purpose, including magnetic coils.

C. Shaft and feedthroughs

The probe shaft, seen in Fig. 3(b), is made out of 2.54 cm in diameter Inconel tubing with pumping openings and features a connector at each end to accommodate the head at the front and the vacuum feedthrough at the back, interconnected by the flexible circuit board.

The Vespel connectors simply sandwich the pins/sockets [Figs. 3(a), 3(c), 5, 6(a), and 6(b)] that are soldered directly to the circuit board, made stiffer at the connector ends for mechanical rigidity purposes. This connection scheme is simple and reliable since it matches directly upon the feedthrough pin configuration without need to cut, peel, bend, redistribute or crimp any cables nor the complexity that accompanies such as scheme (securing the cables, assuring isolation, etc.) resulting in ultracompact 0.75-in.-thick vacuum feedthrough as shown in Fig. 7. Furthermore, the flexibility of the board facilitates assembly as it allows detailed work to be made unhindered [Figs. 8(a), 8(b), 6(b), and 3(a)–3(c)] and then just folds inside the shaft or head upon final assembly. A commercial 21 pin vacuum feedthrough (by Hermetic Seal Corp.) is used at the rear of the probe shaft as show on Figs. 7 and 8(b).

Since the shaft is a mechanically and electrically integrated unit, it can be easily rotated at the rear end by simply loosening the retaining screws that secure the vacuum seal (o-ring based) with the fast bellows and to the pusher assembly that is connected to the fast reciprocating piston, as shown in Fig. 8(b).

IV. PROBE DRIVE

We use a two-stage drive design[6,18,22] where the probe moves powered by a slow step motor and worm screw drive

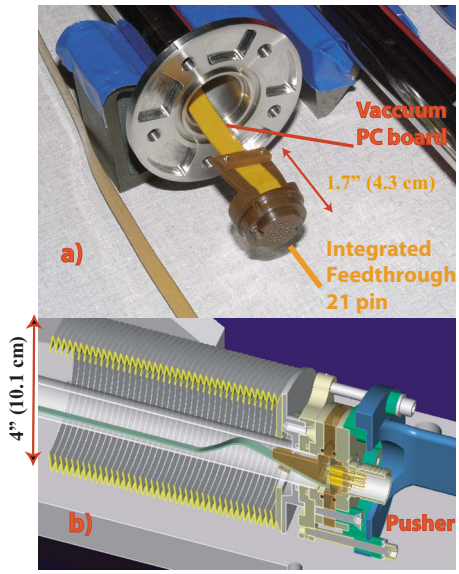

FIG. 8. (Color online) (a) Rear shaft assembly highlighting the flexible board connector and ease of assembly and (b) CAD drawing showing the integrated system with the board pushed inside the shaft. The flexibility of the board is key to the ease of assembly and the compactness of the design.

to a stand-by position where it is close to the plasma, but not exposed to it, and then reciprocates from there rapidly, powered by a fast pneumatic cylinder, when triggered by the control system. The drive mechanism keeps the probe retracted under its own vacuum until needed.

The slow motion section consists of a carriage table fastened to bearing sliders (Thomson Super Bearings), as shown in Figs. 2(a) and 2(b), which moves on a linear track (Thomson Dual Shaft Rail System) fastened to the probe backbone. This section is powered by a Pacific Scientific stepper motor with 92 in.-lb of torque at 72 rpm and operating at 5000 steps/revolution, moving a worm screw. The position of the carriage, measured by a Encoder Products digital encoder producing 500 pulses per revolution, is thus adjustable and can be varied by 30 in. (76.2 cm), determining the deepest penetration of the probe. The worm screw has a pitch of 0.2 in. (0.5 cm) per revolution and is connected to the motor via a 2:1 reducing gear (i.e., 2 motor revolution=1 shaft revolution) equipped with an electromechanical brake for safety. The digital encoder interfaces with the control system and its readout position is continually compared to the final desired position. The absolute probe position is determined with better then 0.01 in. (0.004 cm) accuracy with respect to fiducials inside and outside the vacuum vessel once a year using a FARO arm.

The fast plunge system, consisting of an Aeroquip T-J pneumatic piston powered by helium at 40 psi, valves and bellows, is carried on top of the slow section carriage, as shown in Figs. 2(a) and 2(b). The piston, pushing the probe, reciprocates when the multiple fast valves are triggered by the control system. The valves control the inlet and outlet piston ports thus offering a variable dwell, penetration and trajectory for the probe that can be fully programmed from the control system. The fast plunge length is usually a constant 8 in. (20.3 cm, with reproducibility of $<1\%$) and determined with a 0.005 cm accuracy using a 12-bit digitizer.

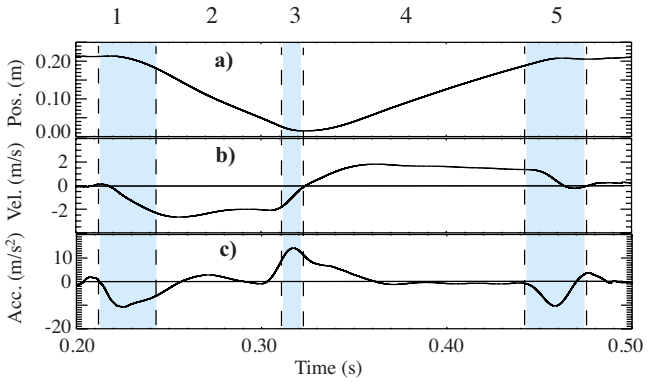

FIG. 9. (Color online) The probe position (a), velocity (b), and acceleration (c) of the probe vs time are shown. Time intervals of interest are marked from 1 to 5. The probe accelerates inward (~ 12 m/s^2) in interval 1, reaches full velocity (2.5–3 m/s) in interval 2, slows down to a stop in interval 3, accelerates back in interval 4 and stops in interval 5.

The position velocity and acceleration of the probe as a function of time are shown in Figs. 9(a)–9(c). The. The intervals of interest are labeled from 1 to 5. In interval 1 the plunge start and the acceleration has a local maximum ($\sim -12g$'s), causing the probe to reach its maximum speed of 2.5 m/s at interval 2. During interval 3, the helium backpressure starts to bring the probe to a halt and the acceleration reaches $\sim 15g$'s. During interval 4, the probe stops briefly and starts moving back at a slightly reduced speed (~ 2 m/s) due to the lower helium pressure and the opposing vacuum forces. It is finally brought to a halt in interval 5, resulting in heavy deceleration ($\sim -10g$). It is important to mention that the substantially higher speed of sound in helium [14] offers improved performance over air and that the use of a gas reservoir to maintain the helium pressure during operation is crucial.

V. CONTROL SYSTEM

The probe system is fully controlled by a commercial PLC (GE Fanuc 90–30) that receives all the input signals from the various probe sensors (limit switches, rotary encoder) and the NSTX Interlock System to determine the probe and facility status. These inputs are combined with a set of rules to maintain facility and personnel safety while protecting the probe.

The operators interface with the PLC via two touch-sensitive terminals (Maple System's HMI530C) that communicate with the PLC via RS 232 interfaces and optical fibers. One terminal is located in the control room and the other in the NSTX test cell, so operators can fully control the probe at either location. The touch-screen terminal features large icons with contextual menus that reduce errors and provide additional information about any control, when requested, to assure accurate and safe operation. Both the terminals and the PLC are fully programmable and industry standard, reducing development time and assuring adaptability to future requirements and prompt replacement and repairs if needed.

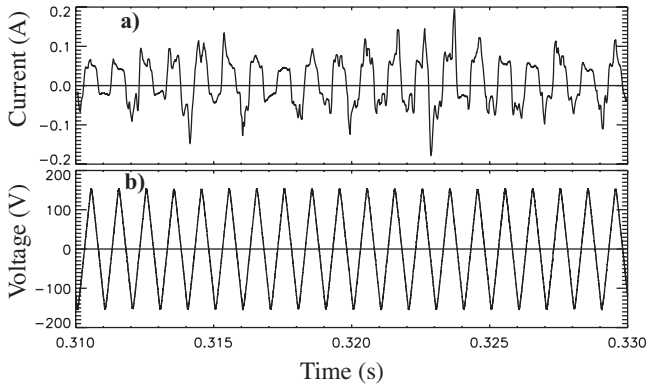

FIG. 10. Traces showing double probe current (a) and voltage (b). The sawtooth voltage sweeps every 1 ms, providing an *I-V* characteristic every 0.5 ms.

VI. REPRESENTATIVE DATA

The probe is located slightly below (8 in. or 20.3 cm) the outer midplane of the machine, where the toroidal magnetic field, B_T, is roughly 2.3 kG during standard operation (magnetic field at axis, $B_T(0) \sim 4$ kG, major radius of magnetic axis, $R_0 \sim 1$ m, major radius of plasma outer midplane, $R_{\mathrm{mid}} \sim 1.5$ m for these discharges) and therefore the size of the ion and electron gyroradius are $\rho_e \sim 5 \times 10^{-3}$ cm, $\rho_i \sim 0.2-0.25$ cm for a range of electron T_e and ion T_i temperatures encountered in the NSTX edge (we assume $T_i \sim T_e$, $\sim T_e \sim 30-100$ eV). The electron gyroradius is smaller than the tip dimensions but the ion gyroradius is comparable ($l \sim 1.6$ mm and $d \sim 1.5$ mm thus $\rho_e < \rho_i \sim d \sim l$) so it is unclear if we operate fully in the magnetized regime and therefore the effective collection area, A_c is ill defined between the full tip area, $A = 2\pi ld/2 \sim 7.5$ mm^2 or the projected area $A_p = 4ld/2 \sim 4.8$ mm^2. Density profiles from the probe and Thomson scattering (TS) were compared while varying the tip collection area to find the best match, which occurs when $A_c \sim 0.05$ cm^2, i.e., the projected area so it seems the probe acts as if in a fully magnetized regime and we will use the projected area A_p of the probe tips as the collection area.[34]

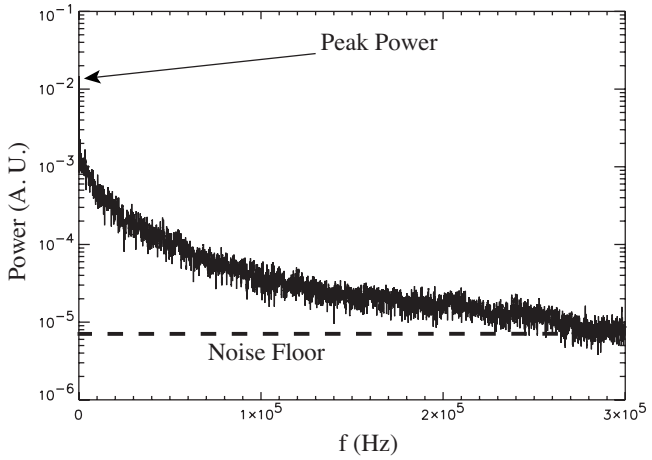

FIG. 11. Power spectrum of the I_{sat} signal sampled near the separatrix and showing that significant fluctuations extend in the 0–200 kHz range. A narrow peak at low frequency (up to $\sim 10-20$ kHz) consists mostly of plasma motion, equilibrium oscillations and magnetohydrodynamics, of no interest for electrostatic turbulent transport and it is usually filtered out.

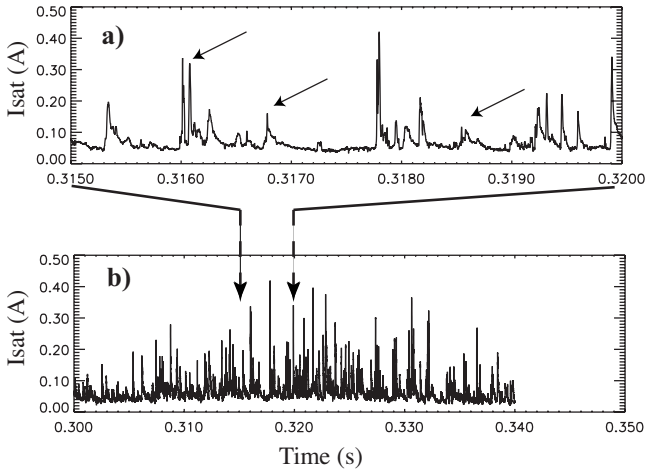

FIG. 12. The I_{sat} trace (b) is shown for a 40 ms interval where the presence of intermittent events is evident. A 5 ms interval (a) is magnified and some intermittent events, which last ~20–40 μs, indicated with arrows.

An important issue is the spatial resolution of the measurements, in the radial direction, the resolution is essentially the tip length (1.6 mm), but toroidally, along the field line, the probe tips collect plasma from–and therefore average over–a certain length along the magnetic field called collection tube whose extent L_p can be estimated[4] if we know the ion perpendicular diffusion coefficient $D_\perp$ and the sound speed c_s by

$$L_p \approx (dlc_s)/(8\ D_\perp).$$

For the values of T_e and T_i given above and using $D_\perp = 0.6-1 \sim m^2/s$ we obtain[35] $L_p \approx 20$ mm. Therefore the data are averaged over ~2.0 cm in the toroidal direction.

The probe measures the saturation current $I_{sat}(t)$ and floating potential V_f, the later at five locations; three separated poloidally and two radially, and therefore we can calculate poloidal $E_\theta(t)$ and radial E_r electric fields and their radial profiles because of the probe movement. The double probe characteristic, thus T_e and n_e, is obtained every 1 ms.

We measure fluctuations at a digitization rate of 1 or 2 MHz (default is 1 MHz, which is shown to be adequate) and the probe system has been designed for, and complies, to a bandwidth of dc −5 MHz. Antialiasing filters are used at either 500 kHz or 1 MHz, depending on the sampling frequency. The conditioning electronics is located near the feedthrough, on top of the probe (Fig. 2) and it is fully shielded electrically and magnetically and the power supplies for the circuitry are separated from the electronics to reduce 60 Hz noise. All connections are coaxial and ~50 Ω all the way from the tip to the digitizer input. The white noise level is low, as can be appreciated in Fig. 11, close to 1–3 orders of magnitude below signal level.

The double probe is swept with a 1 kHz sawtooth voltage of amplitude ±160 V (i.e., 320 V peak-peak) as shown in Fig. 10 in order to provide a full current-voltage (I-V) characteristic every 1 ms. This provides values of the plasma electron density n_e and temperature T_e by fitting the function

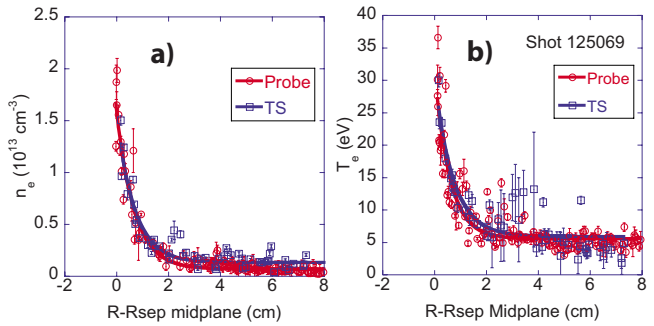

FIG. 13. (Color online) TS (squares) and probe (circles) n_e (plot a), and T_e (plot b) measurements in the SOL are plotted vs R-R_{sep} for discharge 125069. Offset exponential functions are fitted to both measurements (solid lines) as a guide to the eye; excellent agreement is obtained within the scatter.

$$I = I_{sat} \times \tanh(eV_a/2k_bT_e).$$

Here $I_{sat} = 0.5A_p e n_e \sqrt{[k_b(T_e+T_i)]/m_i}$, where we usually assume $T_i \approx T_e$, (which is NOT true in general in the edge plasma but is a good operating assumption since the current is a weak function of the temperature) and V_a is the potential between the probe and the plasma. The double probe has the advantage that it is insensitive to high local potentials since it is a floating system whereas the I_{sat} measurement, a single probe and biased by a power supply referenced to machine ground is liable to lose saturation if the plasma potential itself is highly negative (Figs. 10 and 12).

The signal to noise ratio (S/N) limit varies depending on plasma conditions, but customarily, reliable profiles are obtained up to 6–10 cm out into the SOL, where the low I_{sat} causes excessive sensitivity on the determination of T_e, a derivative. Averaging two or three sweeps can be done in order to improve the S/N ratio in exchange for some loss in spatial resolution. These signals are digitized at 1 MHz to resolve enough points (~500) per sweep to improve fitting convergence. The error of the fitting varies with the sweep rate due to the fact that large density fluctuations (of the

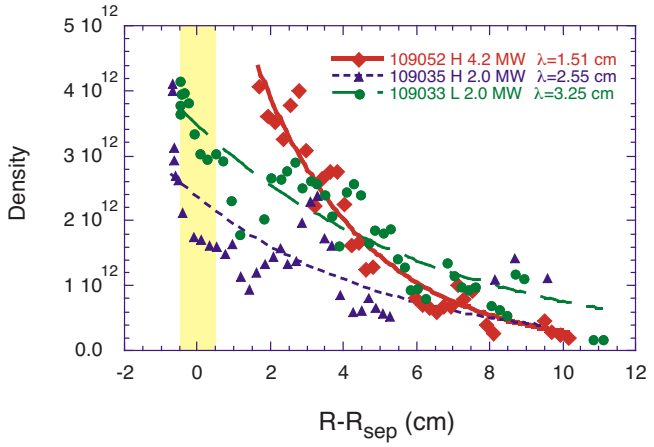

FIG. 14. (Color online) Traces of electron density vs radial position measured by the double probe for three NSTX discharges. The data are labeled by discharge number, confinement regime (L or H confinement) and heating power in MW. An exponential fit and resulting decay length are also indicated for each trace the longest decay length corresponds to an L-mode discharge. The nominal position of the separatrix is labeled zero. The probe penetrates about 7 mm in the plasma core.

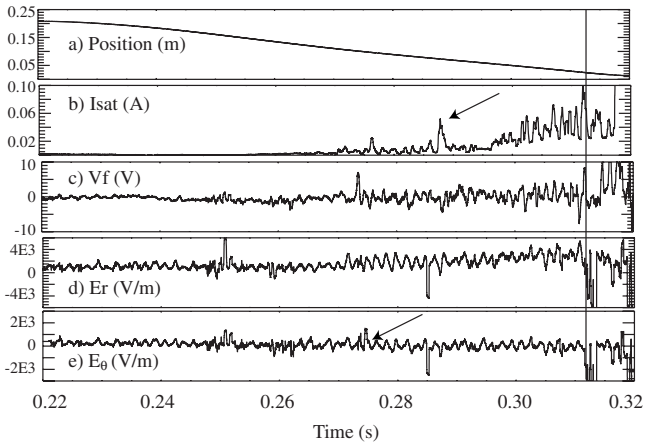

FIG. 15. Traces of: (a) probe position, (b) saturation current (I_{sat}), (c) floating potential (V_f), (d) radial electric field (E_r) and (e) poloidal electric field (E_θ) for a NSTX discharge. Only the inward-traveling part of the plunge is shown. Despite some smoothing, fluctuations and intermittency (one event is marked by a vertical line) can be clearly seen. Arrows indicate intermittent events for guidance. The noise level in the processed signals (E_r, E_θ), seen in the first 20 ms) is higher due to common mode noise and systematic errors.

order of 50%) exist at the plasma edge and it can, therefore be deleterious to sweep too fast since the fluctuations are not averaged over sufficient time.

An additional issue is the presence of plasma intermittency, which consists on fast, bursty events with duration of 30–60 μs, as shown in Figs. 10 and 12 that worsens the S/N ratio and convergence issues. Intermittency is an integral part of the tokamak boundary turbulence, due to interchange instability, and has been observed in a variety of magnetic configurations,[36] tokamaks,[37,15] linear devices, and in NSTX.[38] The intermittency is the result of fast plasma filaments that convect particles and energy rapidly toward the chamber walls.

The radial profiles of all the quantities of interest can be reconstructed from the time-position information. The spatial resolution will depend on the voltage sweep frequency (1 kHz), sampling rate (1 MHz), and the velocity of the probe. At its fastest (2.5 m/s), the probe moves about 1.25 mm during a double probe sweep, i.e., in 0.5 ms, less than the 1.6 mm tip length. So our resolution has a lower limit of 1.6 mm.

We have compared the probe data in the SOL to Thomson scattering (TS) data in Fig. 13 by mapping them in common coordinates. The Thomson n_e and T_e profiles (squares) overlap well with the probe data (circles). The probe penetrates to the separatrix, indicating a density of $\sim 2 \times 10^{19}$ m^{-3} and a temperature of ~ 35 eV. The TS data are integrated over several Thomson pulses to obtain equivalent data density.

Profiles of SOL electron density for three NSTX discharges with different input power, in high (H) and low (L) confinement modes, are shown in Fig. 14. Edge profiles of T_e and n_e are needed as input for codes which model the edge and SOL (Refs. 39 and 13) of tokamak plasmas by solving a set of coupled nonlinear fluid equations, a particle source form the core, a sink from the divertor, and a neutral source. Exponential profiles are expected for simple, sourceless SOL, however, we find that the profiles in the SOL of NSTX are best fitted by offset exponential functions, indicating a local source or faster-than-expected radial transport

$$n_e(r) = n_{e0} + n_e(Rs) \times \exp[-(r - Rs)/\lambda_n],$$

$$T_e(r) = T_{e0} + T_e(Rs) \times \exp[-(r - Rs)/\lambda_T],$$

where R_s is the radius of the last closed flux surface, n_{e0}, T_{e0} are offsets and λ_n, λ_T are the characteristic decay lengths. The fit values for some SOL density profiles in NSTX are shown in Fig. 14 and calculated to a Chi squared of 0.85 or better. Notice that the decay length, longest for a L-mode discharge, at 3.25 cm, is markedly reduced in H mode to 2.55 cm (same input power at 2 MW) and further reduced to 1.51 cm at the highest power H-mode discharge. The SOL decay length is reduced in H mode, as expected and is further reduced by input power in NSTX.

The probe can also provide simultaneous measurements of the fluctuating quantities $\tilde{E}_\theta$ and $\tilde{n}_e$ and from them infer turbulent particle and heat transport as described by Liewer *et al.*[40] and Powers.[41] A representative set of measurements are shown in Fig. 15, where the saturation current I_{sat}, a

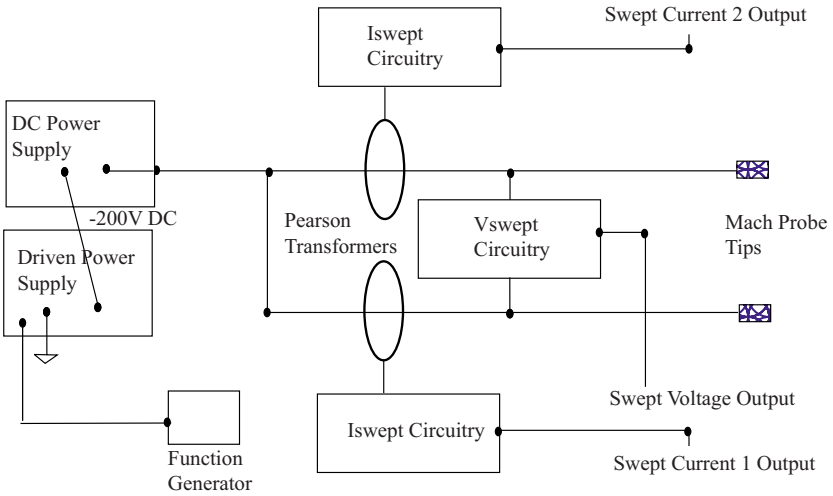

FIG. 16. (Color online) Circuit diagram of the Mach probe (also similar to that of the I_{sat} and double probe) showing the swept power supply (Kepco) arrangement, the current measurement using Pearson transformers. The voltage is measured using Burr–Brown based isolating amplifiers.

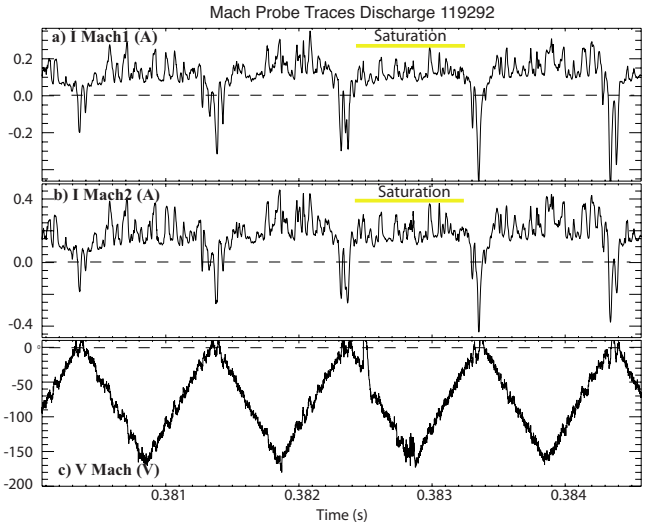

FIG. 17. (Color online) Typical traces of: saturation current (I_{sat}), for the (a) downstream and (b) upstream Mach tips, and (c) the applied voltage. The flattening of the I_{sat} signals, marked in yellow for one sweep, indicates that ion saturation current has been reached.

floating potential V_f, a radial E_r, and poloidal $\tilde{E}_\theta$, electric fields are plotted for a 10 ms interval. A variety of fluctuations are observed, some of them very correlated, indicating some sort of structure in the plasma sampled. The probe system supports a bandwidth of >3 Mhz, although the turbulence features significant power only up to ~200–250 kHz, as seen in Fig. 11, where the noise floor is reached at ~300 kHz.

A Mach probe was also implemented by using two tips located in opposite sides of the isolating BN separator in the probe head (see Fig. 2). A sawtooth voltage is applied in parallel to both tips using a circuitry shown in Fig. 16 and the current for each tip is collected and monitored separately. The traces for voltage and current are shown in Fig. 17, featuring clear saturation of the current for both tips. The Mach number is calculated based on the work by Chung and Hutchinson[42–44] and the resulting profile is shown in Fig. 18. The flow is at Mach ~0.15 toward the nearest divertor and quickly increases as the probe gets closer to the wall into the far SOL due to the proximity of a myriad of structures, such as the nearest wall, antennae, etc.

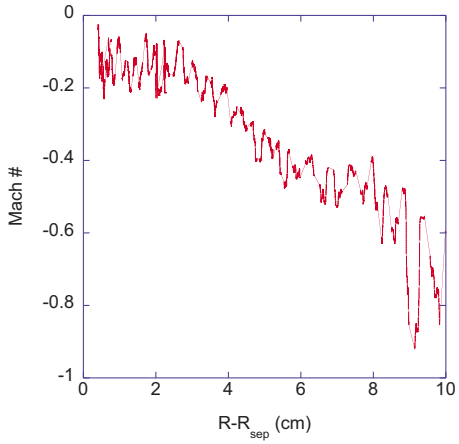

FIG. 18. (Color online) Mach number profile showing a flat, low flow ($M \sim 0.15$) across the near SOL region and increasing toward the wall, mostly due to nearby structures.

VII. SUMMARY

The design of a fast scanning probe for NSTX has been presented. The probe has ~1.6 mm radial resolution and ~3 cm toroidal resolution. The time resolution for T_e and n_e measurements is ~1 ms and for fluctuation measurements is 2 μs. The bandwidth of the system is excellent, showing a good S/N ratio and the ability to resolve fluctuations to 250 kHz, where the plasma electrostatic fluctuation power becomes low and meets the noise floor. Density profiles for L and H-mode plasmas at various powers are shown. The decay length of the profile, varying from 3.2 to 1.5 cm, is clearly reduced by increased power. We have shown profiles of density, temperature under several discharge conditions, fast measurements of various quantities and profiles of the Mach number in the edge.

ACKNOWLEDGMENTS

This work has been supported by the DOE Contract No. DE-FG02-03ER54731. The authors are grateful to the NSTX technical support, to Dr. J-W Ahn, and to UCSD's CER-Fusion Energy Division Technical Support Staff for their assistance support. In particular, we are indebted to G. Mounce and T. Lynch.

[1] S. M. Kaye, M. G. Bell, R. E. Bell, S. Bernabei, J. Bialek, T. Biewer, W. Blanchard, J. Boedo, C. Bush, M. D. Carter, W. Choe, N. Crocker, D. S. Darrow, W. Davis, L. Delgado-Aparicio, S. Diem, J. Ferron, A. Field, J. Foley, E. D. Fredrickson, D. A. Gates, T. Gibney, R. Harvey, R. E. Hatcher, W. Heidbrink, K. Hill, J. C. Hosea, T. R. Jarboe, D. W. Johnson, R. Kaita, C. Kessel, S. Kubota, H. W. Kugel, J. Lawson, B. P. LeBlanc, K. C. Lee, F. Levinton, R. Maingi, J. Manickam, R. Maqueda, R. Marsala, D. Mastrovito, T. K. Mau, S. S. Medley, J. Menard, H. Meyer, D. R. Mikkelsen, D. Mueller, T. Munsat, B. A. Nelson, C. Neumeyer, N. Nishino, M. Ono, H. Park, W. Park, S. Paul, T. Peebles, M. Peng, C. Phillips, A. Pigarov, R. Pinsker, A. Ram, S. Ramakrishnan, R. Raman, D. Rasmussen, M. Redi, M. Rensink, G. Rewoldt, J. Robinson, P. Roney, A. L. Roquemore, E. Ruskov, P. Ryan, S. A. Sabbagh, H. Schneider, C. H. Skinner, D. R. Smith, A. Sontag, V. Soukhanovskii, T. Stevenson, D. Stotler, B. Stratton, D. Stutman, D. Swain, E. Synakowski, Y. Takase, G. Taylor, K. Tritz, A. von Halle, M. Wade, R. White, J. Wilgen, M. Williams, J. R. Wilson, W. Zhu, S. J. Zweben, R. Akers, P. Beiersdorfer, R. Betti, T. Bigelow, M. Bitter, P. Bonoli, C. Bourdelle, C. S. Chang, J. Chrzanowski, C. Domier, L. Dudek, P. C. Efthimion, M. Finkenthal, E. Fredd, G. Y. Fu, A. Glasser, R. J. Goldston, N. L. Greenough, L. R. Grisham, N. Gorelenkov, L. Guazzotto, R. J. Hawryluk, J. Hogan, W. Houlberg, D. Humphreys, F. Jaeger, M. Kalish, S. Krasheninnikov, L. L. Lao, J. Lawrence, J. Leuer, D. Liu, N. C. Luhmann, E. Mazzucato, G. Oliaro, D. Pacella, R. Parsells, M. Schaffer, I. Semenov, K. C. Shaing, M. A. Shapiro, K. Shinohara, P. Sichta, X. Tang, R. Vero, D. Walker, and W. Wampler, Nucl. Fusion **45**, S168 (2005).
[2] M. Ono, M. Peng, C. Kessel, C. Neumeyer, J. Schmidt, J. Chrzanowski, D. Darrow, L. Grisham, P. Heitzenroeder, T. Jarboe, C. Jun, S. Kaye, J. Menard, R. Raman, T. Stevenson, M. Viola, J. Wilson, R. Woolley, and I. Zatz, Nucl. Fusion **44**, 452 (2004).
[3] P. C. Stangeby and G. M. McCracken, Nucl. Fusion **30**, 1225 (1990).
[4] S. I. Itoh, K. Itoh, M. Yagi, and A. Fukuyama, Plasma Phys. Controlled Fusion **38**, 1743 (1996).
[5] Ch. Ritz, H. Lin, T. L. Rhodes, and A. J. Wooton, Phys. Rev. Lett. **65**, 2543 (1990).
[6] Ch. P. Ritz, R. V.. Bravenec, P. M. Schoch, R. D. Bengtson, J. A. Boedo, J. C. Foster, K. W. Gentle, Y. He *et al.*, Phys. Rev. Lett. **62**, 1844 (1989).
[7] W. L. Rowan, C. C. Klepper, and C. P. Ritz, Nucl. Fusion **27**, 1105 (1987).

[8] G. R. Tynan, L. Schmitz, L. Blush, J. A. Boedo, R. W. Conn, R. Doerner, R. Lehmer, R. Moyer, H. Krugel, R. Bell, S. Kaye, M. Okabayashi, S. Sesnic, and Y. Sun, Phys. Plasmas **1**, 3301 (1994).
[9] T. L. Rhodes, C. P. Ritz, and R. D. Bengtson, Nucl. Fusion **33**, 1147 (1993).
[10] P. C. Stangeby, J. D. Elder, J. A. Boedo, B. Bray, N. H. Brooks, M. E. Fenstermacher, M. Groth, R. C. Isler, L. L. Lao, S. Lisgo, G. D. Porter, D. Reiter, D. L. Rudakov, J. G. Watkins, W. P. West, and D. G. White, J. Nucl. Mater. **313–316**, 883 (2003).
[11] X. Q. Xu, R. H. Cohen, W. M. Nevins, G. D. Porter, M. E. Rensink, T. D. Rognlien, J. R. Myra, D. A. D'Ippolito, R. A. Moyer, P. B. Snyder, and T. N. Carlstrom, Nucl. Fusion **42**, 21 (2002).
[12] G. D. Porter, R. Isler, J. Boedo, and T. D. Rognlien, Phys. Plasmas **7**, 3663 (2000).
[13] A. S. Kukushkin, H. D. Pacher, G. W. Pacher, G. Janeschitz, D. Coster, A. Loarte, and D. Reiter, Nucl. Fusion **43**, 716 (2003).
[14] D. Reiter, S. Wiesen, and M. Born, J. Nucl. Mater. **313–316**, 845 (2003).
[15] J. A. Boedo, D. Rudakov, R. Moyer, S. Krasheninnikov, D. Whyte, G. McKee, G. Tynan, M. Schaffer, P. Stangeby, P. West, S. Allen, T. Evans, R. Fonck, E. Hollmann, A. Leonard, A. Mahdavi, G. Porter, M. Tillack, and G. Antar, Phys. Plasmas **8**, 4826 (2001).
[16] J. G. Watkins, J. Salmonson, R. Moyer, R. Doerner, R. Lehmer, L. Schmitz, and D. N. Hill, Rev. Sci. Instrum. **63**, 4728 (1992).
[17] T. L. Rhodes, C. P. Ritz, R. D. Bengtson, and K. R. Carter, Rev. Sci. Instrum. **61**, 3001 (1990).
[18] G. R. Tynan, J. Liberati, P. Pribyl, and B. Wells, Plasma Phys. Controlled Fusion **38**, 1301 (1996).
[19] J. G. Watkins, J. Hunter, B. Tafoya, M. Ulrickson, R. D. Watson, R. A. Moyer, J. W. Cuthbertson, G. Gunner, R. Lehmer, P. Luong, D. N. Hill, M. Mascaro, J. I. Robinson, R. Snider, and R. Stambaugh, Rev. Sci. Instrum. **68**, 373 (1997).
[20] J. A. Boedo, D. Gray, L. Chousal, R. Conn, B. Hiller, and K. H. Finken, Rev. Sci. Instrum. **69**, 2663 (1998).
[21] B. LaBombard, J. Goetz, C. Kurz, D. Jablonski, B. Lipschultz, G. McCracken, A. Niemczewski, R. L. Boivin, F. Bombarda, C. Christensen, S. Fairfax, C. Fiore, D. Garnier, M. Graf, S. Golovato, R. Granetz, M. Greenwald, S. Horne, A. Hubbard, I. Hutchinson, J. Irby, J. Kesner, T. Luke, E. Marmar, M. May, P. O'Shea, M. Porkolab, J. Reardon, J. Rice, J. Schachter, J. Snipes, P. Stek, Y. Takase, J. Terry, G. Tinios, R. Watterson, B. Welch, and S. Wolfe, Phys. Plasmas **2**, 2242 (1995).
[22] N. Smick, B. La Bombard, and C. S. Pitcher, J. Nucl. Mater. **337–339**, 281 (2005).
[23] MAST team, Y. Yang, and G. F. Counsell, J. Nucl. Mater. **313–316**, 734 (2003).
[24] O. E. Garcia, J. Horacek, R. A. Pitts, A. H. Nielsen, W. Fundamenski, J. P. Graves, V. Naulin, and J. J. Rasmussen, Plasma Phys. Controlled Fusion **48**, L1 (2006).
[25] C. Silva, B. Goncalves, C. Hidalgo, M. A. Pedrosa, K. Erents, G. Matthews, and R. A. Pitts, Rev. Sci. Instrum. **75**, 4314 (2004).
[26] R. A. Pitts, R. Chavan, S. J. Davies, S. K. Erents, G. Kaverney, G. F. Matthews, G. Neill, J. E. Vince, and I. Duran, Rev. Sci. Instrum. **74**, 4644 (2003).
[27] M. Tsalas and N. Tsois, Proceedings of the EPS Conference ECA, 2005 (unpublished), Vol. 29C, p. 001.
[28] H. Mueller and V. Bobkov, Proceedings of the EPS Conference ECA, 2005 (unpublished), Vol. 29C, p. 1.009.
[29] C. S. Pitcher, P. C. Stangeby, R. V. Budny, C. E. Bush, J. D. Edler, S. J. Kilpatrick, D. M. Manos, S. S. Medley, A. T. Ramsey, J. F. Schivell, and M. Ulrickson, Nucl. Fusion **32**, 239 (1992).
[30] S. J. Kilpatrick, C. S. Pitcher, M. G. Bell, D. M. Manos, D. K. Mansfield, I. Nyberg, A. T. Ramsey, and B. C. Stratton, J. Vac. Sci. Technol. A **8**, 1767 (1990).
[31] D. M. Manos, R. V. Budny, S. Kirkpatrick, P. Stangeby, and S. Zweben, Rev. Sci. Instrum. **57**, 2107 (1986).
[32] C. Neumeyer, P. Heitzenroeder, J. Spitzer, J. Chrzanowski, A. Brooks, J. Bialek, E. Perry, T. Egebo, A. Von Halle, M. Williams, and M. Ono, Fusion Eng. Des. **54**, 275 (2001).
[33] P. W. Hait, Proceedings of the 13th Vacuum Symposium of the American Vacuum Society, 1996 (unpublished), Vol. 1, p. 678.
[34] R. Pitts *et al.*, Nucl. Fusion 789 (1990).
[35] D. S. Gray, M. Baelmans, J. A. Boedo, and R. W. Conn, Phys. Plasmas **6**, 2816 (1999).
[36] A. H. Nielsen, H. L. Pecsell, and J. Juul Rasmussen, Phys. Plasmas **3**, 1530 (1996).
[37] R. A. Moyer, R. D. Lehmer, T. E. Evans, R. W. Conn, and L. Schmitz, Plasma Phys. Controlled Fusion **38**, 1273 (1996).
[38] L. Colas, L. Costanzo, C. Desgranges, S. Bremond, J. Bucalossi, G. Agarici, V. Basiuk, B. Beaumont, A. Becoulet, and F. Nguyen, Nucl. Fusion **43**, 1 (2003).
[39] M. Baelmans, D. Reiter, R. R. Weynants *et al.*, J. Nucl. Mater. **1**, 446 (1992).
[40] P. C. Liewer, J. M. McChesney, S. J. Zweben, and R. W. Gould, Phys. Fluids **29**, 309 (1986).
[41] E. J. Powers, Nucl. Fusion **14**, 749 (1974).
[42] K. S. Chung and I. H. Hutchinson, Phys. Rev. A **38**, 4721 (1988).
[43] K. S. Chung and I. H. Hutchinson, Phys. Fluids B **3**, 3053 (1991).
[44] K. S. Chung, Phys. Plasmas **1**, 2864 (1994).